Comput Mech (2016) 58:1003–1018
DOI 10.1007/s00466-016-1328-5

ORIGINAL PAPER

A novel two-stage discrete crack method based on the screened Poisson equation and local mesh refinement

P. Areias[1,4] · **T. Rabczuk**[2] · **J. César de Sá**[3]

Received: 23 May 2016 / Accepted: 4 September 2016 / Published online: 22 September 2016

Abstract We propose an alternative crack propagation algorithm which effectively circumvents the variable transfer procedure adopted with classical mesh adaptation algorithms. The present alternative consists of two stages: a mesh-creation stage where a local damage model is employed with the objective of defining a crack-conforming mesh and a subsequent analysis stage with a localization limiter in the form of a modified screened Poisson equation which is exempt of crack path calculations. In the second stage, the crack naturally occurs within the refined region. A staggered scheme for standard equilibrium and screened Poisson equations is used in this second stage. Element subdivision is based on edge split operations using a constitutive quantity (damage). To assess the robustness and accuracy of this algorithm, we use five quasi-brittle benchmarks, all successfully solved.

Keywords Two-stage algorithm · Local mesh refinement · Smeared model · Crack nucleation and propagation · Quasi-brittle fracture

1 Introduction

For equilibrium problems, the presence of cracks causes the displacement field to be discontinuous in the normal to the crack faces. Finite element polynomial interpolation is inadequate for the representation of discontinuous functions. This fact has encouraged the development of methods explicitly introducing a discontinuity in the interpolation functions [1,2]. These methods entail technical challenges in terms of generalization and have intricate coding requirements. However, it is also established that, if local solution accuracy is not the primary objective of an analysis (i.e. singular stress fields) there is no demand for specific treatment of the standard displacement-based solution to calculate the J-integral (cf. [3]). From the energy balance perspective (specifically localized strain energy density loss), displacement discontinuities can be replaced by inactive elements or explicit boundaries. In alternative, localization limiters (cf. [4]) with strain softening constitutive laws allow a similar effect. Existing techniques for computational fracture can be classified as either discrete or continuum-based:

- Remeshing procedures with extraneous crack path determination [5,6], local displacement [1,7–11] and strain [2,12] enrichments, clique overlaps [13], edges repositioning [14] and edge-based fracture with R-adaptivity [15]. Duflot and Nguyen-Dang [16] successfully introduced the near-tip Westergaard field in moving least-squares meshless weight functions, which parallels the extended finite element developments. Another recent meshless discretization based on discontinuous kernels was proposed by Barbieri and Petrinic [17]. Peng et al. [18] recently proposed an isogeometric/boundary element method where NURBS patches are used to discretize the crack surfaces. Element cutting by topological operations

✉ P. Areias
pmaa@uevora.pt

[1] Department of Physics, University of Évora, Colégio Luís António Verney Rua Romão Ramalho, 59, 7002-554 Évora, Portugal

[2] Institute of Structural Mechanics, Bauhaus-University Weimar, Marienstraße 15, 99423 Weimar, Germany

[3] Mechanical Engineering, Department Faculty of Engineering, University of Porto, Rua Dr. Roberto Frias, s/n, 4200-465 Porto, Portugal

[4] CERIS/Instituto Superior Técnico, University of Lisbon, Lisbon, Portugal

was recently proposed by Paulus et al. [19]. Full remeshing techniques have also been used with some degree of success (see the work of Bouchard [20,21]);
- Fixed-mesh element erosion [22], smeared band algorithms [23], viscous-regularized techniques [24], gradient and non-local continua [25].

We aim robustness and generality (cf. [26]) with respect to element technology and opt to use a purely constitutive algorithm which produces a damage value that also serves as an indicator of material collapse. This has been titled "*continuum approach to fracture*" [27] and we explore it in this work. With this approach, pre-cracks or pre-notches are unnecessary and explicit calculation of crack paths is not performed. Regularization is adopted in the form of a staggered algorithm for the strain with the screened Poisson equation (see, e.g. [28]) here with a modified version. To ensure a reasonable solution and corresponding crack path, we use a preliminary stage with local remeshing. A two-stage algorithm is therefore introduced:

1. The first stage uses a standard local equilibrium analysis with recursive local remeshing, node repositioning and variable transfer. The analysis is performed without a localization limiter, as the only objective is to produce an appropriate mesh.
2. After unloading, the mesh obtained from the first stage is used in a staggered algorithm using equilibrium equations and the screened Poisson equation.

Results produced by the present algorithm show that this is able to achieve:

- Very good mesh-size independence.
- Excellent length-scale independence for values compatible with the mesh size.
- Moderate step-size independence.
- Reproduction of curved crack paths.
- Successful application to demanding quasi-brittle problems.

2 Governing equations: constitutive integration in finite strains

Using standard notation, we write the spatial equilibrium equations as [29]:

$$\frac{\partial \sigma_{ij}}{\partial x_j} + b_i = 0 \tag{1}$$

with the Cauchy tensor components σ_{ij} $(i, j = 1, 2, 3)$. In (1) i is the direction index and j is the facet index. The components of the body force vector are b_i. In (1), coordinates x_j are the spatial, or deformed, coordinates of a given point under consideration. In addition, the following natural and essential boundary conditions hold on each part of the boundary $\Gamma = \Gamma^t \cup \Gamma^u$ where Γ^t is the natural boundary and Γ^u is the essential boundary:

$$\bar{\boldsymbol{t}} = \boldsymbol{\sigma} \cdot \boldsymbol{v} \quad \text{on} \quad \Gamma^t \tag{2}$$

$$\bar{\boldsymbol{u}} = \boldsymbol{u} \quad \text{on} \quad \Gamma^u \tag{3}$$

where $\bar{\boldsymbol{t}}$ is the known stress vector on Γ^t where $\boldsymbol{v}$ is the outer normal and $\bar{\boldsymbol{u}}$ is the known displacement field on Γ^u. It is assumed that (1) and (2–3) are satisfied for a time parameter $t \in [0, T]$ with T being the total time of analysis and for a point with position $\boldsymbol{x} \in \Omega$ belonging to the deformed position domain at the time of analysis. Natural boundary Γ^t is evolving in the sense that cracks create boundaries with known $\bar{\boldsymbol{t}}$. Equilibrium configuration corresponds to the domain Ω. In tensor notation, Eq. (1) can be presented as:

$$\nabla \cdot \boldsymbol{\sigma}^T + \boldsymbol{b} = \boldsymbol{0} \tag{4}$$

with $\nabla = \partial/\partial\boldsymbol{x}$ being the spatial gradient *operator*. After multiplication by the velocity field $\dot{\boldsymbol{u}}$, integration in the deformed configuration Ω and application of integration by parts component-wise, we obtain the following power form ($\dot{W}_{\text{int}}$ is the internal and $\dot{W}_{\text{ext}}$ is the external power):

$$\underbrace{\int_\Omega \boldsymbol{\sigma} : \boldsymbol{L} \mathrm{d}\Omega}_{\dot{W}_{\text{int}}} = \underbrace{\int_\Omega \boldsymbol{b} \cdot \dot{\boldsymbol{u}} \mathrm{d}\Omega + \int_{\Gamma^t} \bar{\boldsymbol{t}} \cdot \dot{\boldsymbol{u}} \mathrm{d}\Gamma}_{\dot{W}_{\text{ext}}} \tag{5}$$

where $\boldsymbol{L}$ is the velocity gradient: $\boldsymbol{L} = \frac{\partial \dot{\boldsymbol{x}}}{\partial \boldsymbol{x}} = \frac{\partial \dot{\boldsymbol{u}}}{\partial \boldsymbol{x}}$. Using the undeformed configuration Ω_0 for the left-hand side, it is well known that (5) can be written as:

$$\underbrace{\int_{\Omega_0} \boldsymbol{S} : \dot{\boldsymbol{E}} \mathrm{d}\Omega_0}_{\dot{W}_{\text{int}}} = \underbrace{\int_\Omega \boldsymbol{b} \cdot \dot{\boldsymbol{u}} \mathrm{d}\Omega + \int_{\Gamma^t} \bar{\boldsymbol{t}} \cdot \dot{\boldsymbol{u}} \mathrm{d}\Gamma}_{\dot{W}_{\text{ext}}} \tag{6}$$

where $\boldsymbol{S}$ is the second Piola-Kirchhoff stress and $\boldsymbol{E}$ is the corresponding Green-Lagrange tensor. Eigenvalues of $\boldsymbol{E}$ are identified as ε_1, ε_2 and ε_3. For the quasi-brittle model employed in this work, we use the Mazars [30] definition of equivalent strain, here denoted ε_{eq}:

$$\varepsilon_{\text{eq}} = \sqrt{\sum_{i=1}^{3} \langle \varepsilon_i \rangle^2} \tag{7}$$

with $\langle \varepsilon_i \rangle = \frac{\varepsilon_i + |\varepsilon_i|}{2}$, $i = 1, 2, 3$. From (7) the maximum equivalent strain ε is defined as $\varepsilon = \max_{\text{hist}} \left[\varepsilon_{\text{eq}}\right]$. With a non-local representation of ε, which is denoted $\overline{\varepsilon}$ we use a strict approach: only the softening function depends on $\overline{\varepsilon}$. Note that in the literature, ε_{eq} is frequently adopted for the nonlocal strain approach, e.g. [31]. Loading/unloading conditions strictly involve local quantities and the structure of the local constitutive representation remains. Defining the equivalent stress as $\sigma_{\text{eq}} = E\varepsilon_{\text{eq}}$ and introducing a softening function $\overline{\sigma}(\overline{\varepsilon})$, we establish the loading/unloading conditions in terms of stress:

$$(1-d)\,\sigma_{\text{eq}} - \overline{\sigma}(\overline{\varepsilon}) \leq 0 \tag{8}$$

$$\dot{d} \geq 0 \tag{9}$$

$$\dot{d}\left[(1-d)\,\sigma_{\text{eq}} - \overline{\sigma}(\overline{\varepsilon})\right] = 0 \tag{10}$$

from which a Hookean-like constitutive law is obtained, where Voigt notation is used:

$$\mathbf{S} = (1-d)\,\mathscr{C}\mathbf{E} \tag{11}$$

and $\mathscr{C}$ is the elastic tangent modulus. Function $\overline{\sigma}(\overline{\varepsilon})$ follows the standard exponential softening law:

$$\overline{\sigma}\,(\overline{\varepsilon}) = \sigma_{\max} \exp\left[-\frac{\overline{\varepsilon} L \sigma_{\max}}{G_c}\right] \tag{12}$$

In (12), $\sigma_{\max}$ is the maximum equivalent stress, G_c is the critical strain energy release rate (all modes are equally combined in ε_{eq}) and L is the length scale parameter. To ensure consistence with other models, we identify d in (8–10) and (11) as the damage constitutive variable. Implementation details, including the control equation for the solution, are provided in previous papers, see e.g. [32].

3 Regularization with the screened Poisson equation

The classical screened Poisson equation [28] (typically named Helmholtz-like, cf. [31,33]) is adopted to regularize the otherwise ill-posed equilibrium problem in the presence of strain softening [34]. Using an additional field, $\overline{\varepsilon}$, we perform a coupling with the constitutive-based ε as:

$$l(d, L_m)^2 \left(\nabla_b^2 \overline{\varepsilon}\right) : \boldsymbol{I} = \overline{\varepsilon} - \varepsilon \tag{13}$$

with the following boundary condition:

$$\nabla_b \overline{\varepsilon} \cdot v = 0 \quad \text{in } \Gamma_b \tag{14}$$

A version with constant l was established by Lasry and Belytschko [4] who used an explicit version of this model, requiring higher-order continuity. In (13), ∇_b^2 is the Laplacian with respect to the coordinates in *equilibrium* configuration Ω_b, corresponding to an updated-Lagrangian formulation. This allows the diffusion effect of (13) without the well-known [33] flattening side-effect. It is worth noting that $\overline{\varepsilon}$ given by equation (13) is a weighted average (see [31,35]) and therefore mesh size only affects the local quantity ε which is not directly responsible for softening, as d is made dependent on $\overline{\varepsilon}$. In the present work we introduce the following function $l(d, L_{\text{m}})$:

$$l(d, L_{\text{m}}) = L - dL_{\text{m}}$$

where L_{m} is the average mesh edge size at the localization region. The following constraint applies:

$$L_{\text{m}} \leq L$$

this limits the spreading of the damaged region which occurs with fixed l. An alternative approach with similar effect was used by Geers et al. [35] by means of a rate effect. For the beam example, see Sect. 5.1, two independent equations are used for the lower and upper faces $\overline{\varepsilon}_{\text{lower}}$ and $\overline{\varepsilon}_{\text{upper}}$, respectively:

$$(L - dL_{\text{m}})^2 \left(\nabla_b^2 \overline{\varepsilon}_{\text{lower}}\right) : \boldsymbol{I} = \overline{\varepsilon}_{\text{lower}} - \varepsilon_{\text{lower}} \tag{15}$$

$$(L - dL_{\text{m}})^2 \left(\nabla_b^2 \overline{\varepsilon}_{\text{upper}}\right) : \boldsymbol{I} = \overline{\varepsilon}_{\text{upper}} - \varepsilon_{\text{upper}} \tag{16}$$

We use a staggered scheme to regularize the strain-softening problem. We introduce an element that implements Eq. (13) using the following weak form with the previous rate notation:

$$\dot{W}_\varepsilon = \int_{\Omega_b} \left[-(L - dL_{\text{m}})^2 \left(\nabla_b \overline{\varepsilon} \cdot \nabla_b \dot{\overline{\varepsilon}}\right) + (\varepsilon - \overline{\varepsilon})\,\dot{\overline{\varepsilon}}\right] \mathrm{d}\Omega_b \tag{17}$$

where, in terms of discretization for a triangle, $\overline{\varepsilon} = \sum_{K=1}^{3} N_K(\boldsymbol{\xi})\overline{\varepsilon}_K$ where $N_K(\boldsymbol{\xi})$ are the classical shape functions and $\overline{\varepsilon}_K$ are the nodal unknowns for the regularization element. Linearization of (17) follows:

$$\mathrm{d}\dot{W}_\varepsilon = \int_{\Omega_b} \left[-(L - dL_{\text{m}})^2 \left(\nabla_b \mathrm{d}\overline{\varepsilon} \cdot \nabla_b \dot{\overline{\varepsilon}}\right) - \mathrm{d}\overline{\varepsilon}\dot{\overline{\varepsilon}}\right] \mathrm{d}\Omega_b \tag{18}$$

We omit the case for a plate or shell, as it constitutes a simple extension of (17) and (18). The implementation is performed with Mathematica [36] and AceGen software [37]. We obtain the following element residual for node M:

$$\begin{aligned} r_M^e = \int_{\Omega_b} \Bigg[&-(L - dL_{\text{m}})^2 \frac{\partial N_K}{\partial x_i} \frac{\partial N_M}{\partial x_i} \overline{\varepsilon}_K \\ &+ (\varepsilon - N_K \overline{\varepsilon}_K)\, N_M \Bigg] \mathrm{d}\Omega_b = 0 \end{aligned} \tag{19}$$

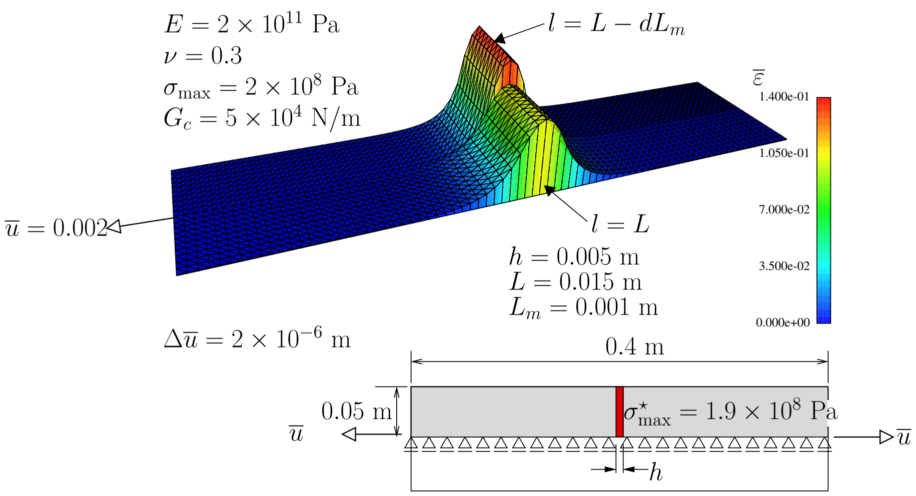

Fig. 1 Stretched bar under tension: localization region as a function of $\bar{\varepsilon}$ for $l = L$ and $l = L - dL_m$. (Color figure online)

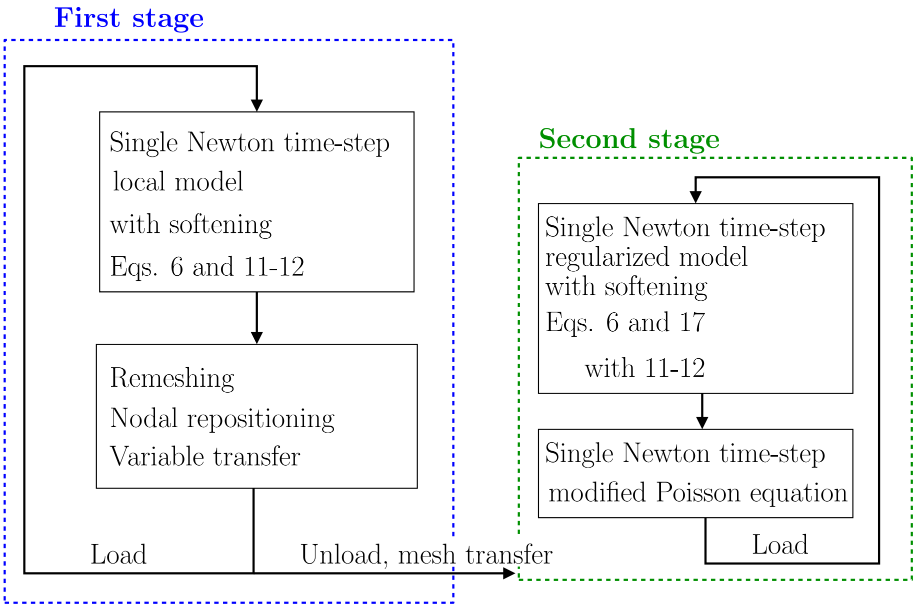

Fig. 2 Two-stage algorithm for crack propagation

where the sum symbol for K was omitted. In (19), N_K are the shape functions. The linearization corresponding to (19) provides the element stiffness matrix for nodes M and K as:

$$K^e_{MK} = \int_{\Omega_b} \left[-(L - dL_{\mathrm{m}})^2 \frac{\partial N_K}{\partial x_i} \frac{\partial N_M}{\partial x_i} - N_K N_M \right] \mathrm{d}\Omega_b \tag{20}$$

To compare this new technique with the conventional fixed-l algorithm, we compare the localization regions in tension for a stretched bar in Fig. 1 where all relevant data is shown. We can observe that our new technique with variable l results in a much sharper definition of the localization region.

4 Element subdivision and repositioning algorithm

We use two stages, depicted in Fig. 2:

1. In the first stage a local approach to fracture, known to be ill-posed, cf. [38], whose only purpose in this context is to provide, along with the remeshing algorithm herein described, a locally refined mesh for the second stage.
2. We subsequently unload the final state of the first stage keeping the new mesh and solve a regularized problem which constitutes the actual fracture analysis. In this stage, the mesh remains fixed.

Since in the second stage no variable transfer occurs and the equations correspond to a regularized problem, results

Algorithm 1 Localized remeshing Algorithm.

```
Mark edges for splitting based on a convex interpolation of $d$ (Fig. 3)
Mark edges for splitting based on the aspect ratio of adjacent elements (Fig. 3)
Create new nodes in the center of marked edges (Fig. 4)
Create new elements by subdivision of elements with marked edges (Fig. 4)
Perform nodal repositioning
Map degrees-of-freedom and history variables for the new mesh
```

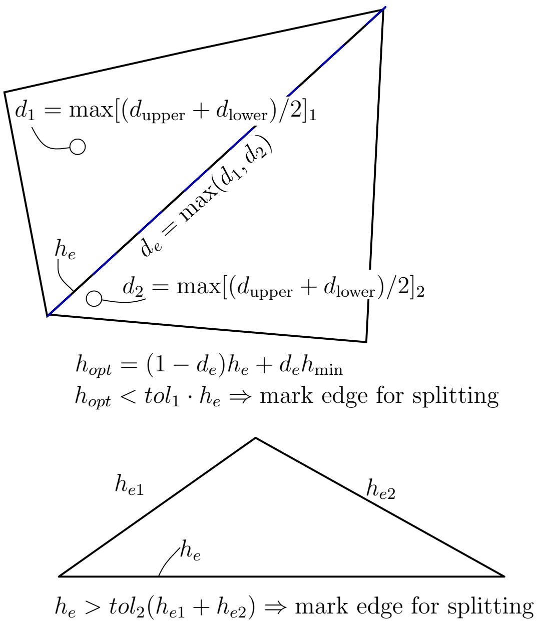

Fig. 3 Splitting based on d and aspect ratio

are very smooth and naturally follow the localization regions determined in the first stage. In the first stage, we use a combination of a simple element subdivision scheme with nodal repositioning, identified as Algorithm 1. Three major steps are performed (1. edge marking, 2. node and element creation, 3. mesh smoothing and mapping). Splitting edges is simpler than rotating edges (cf. [14]) and duplicating tip nodes since no specific crack path tracking is required. We classify each edge according to the maximum value of this mean d for both adjacent elements, cf. 3. An optimal length h_{opt} is defined and, if it is smaller than the actual edge length h_e, the edge is marked for splitting. Concerning the tolerances, Table 1 shows typical values which are used in this work. After all edges are marked for splitting, each element containing at least one marked edge is analyzed for subdivision according to the scheme of Fig. 4: one, two or three divided edges result in one, two or three *additional* elements.

For node repositioning, we adopt an algorithm based on the weighted Laplacian method (cf. [39]) where length ratios are weights:

$$\boldsymbol{x}_K = \frac{1}{\sum_{I=1}^{N_n} \alpha_{KI}} \sum_{I=1}^{N_n} \alpha_{KI} \boldsymbol{x}_{KI} \tag{21}$$

where I is a given node number connected to node K by an element, N_n is the number of nodes connected to K, and

$$\alpha_{KI} = \frac{\|\boldsymbol{x}_I - \boldsymbol{x}_K\|}{\|\boldsymbol{x}_I - \boldsymbol{x}_K\|(1 - \zeta_I) + h_{\min}\zeta_I} \tag{22}$$

$$\zeta_I = d_{\max}^I \tag{23}$$

where $d_{\max}^I$ is the maximum damage variable in all elements sharing node I.

In the first stage, variable mapping is required between meshes. Here it is strictly geometric and consists of the following two tasks:

- Finding the element in the previous mesh where the centroid of *each element* in the current mesh falls. Then *copy* the constitutive history data.
- Finding the element in the previous mesh where each node of the current mesh falls. Then *interpolate* the degrees-of-freedom.

5 Numerical tests

5.1 Shell discretization of a cantilever beam bending with quasi-brittle behavior

The first stage of the proposed algorithm, which includes a modified screened-Poisson equation and a staggered algorithm is now assessed in its basic features. The modification of the original screened-Poisson equation also modifies the localization behavior. The staggered algorithm must be inspected with respect to drifting of results. We are also concerned with hypothetical spurious diffusion caused by large number of steps. Therefore, a cantilever beam is introduced where all these aspects can be judged without remeshing, which is used in subsequent examples. In summary, the objectives of the simple numerical test (described in Fig. 5) are:

- To assess the dependence of mesh size in the displacement/reaction results. In this case the parameter h shown in Fig. 5 is used. Triangular elements are compared with quadrilaterals.
- To assess the effect on step size in the displacement/reaction results. Refering to Fig. 5, the parameter Δw is used.
- To study the relation between the length parameter L and the element size h.

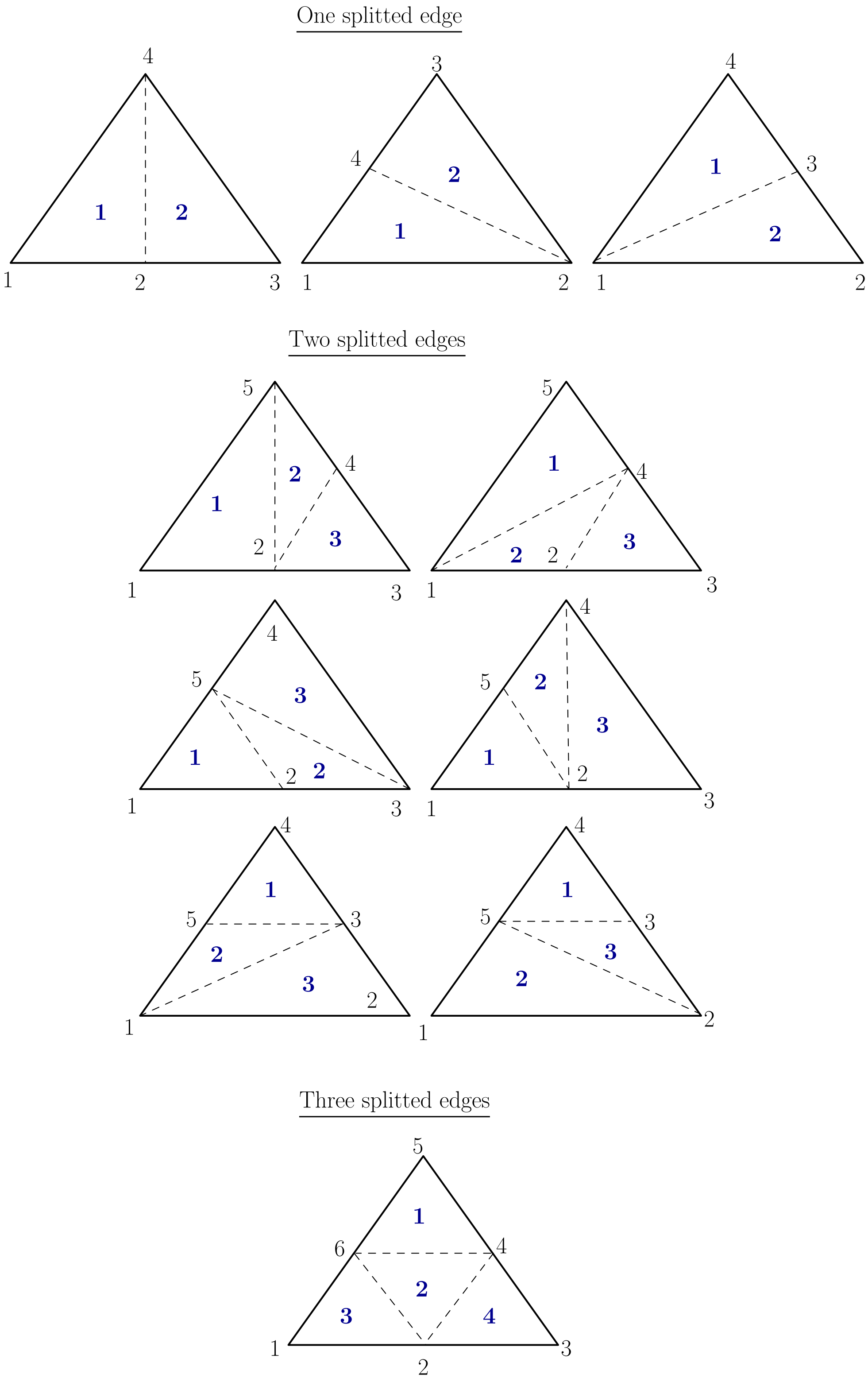

Fig. 4 Element division algorithm based on edge splitted. In *bold* local element numbers

Table 1 Typical values of the parameters for the localized remeshing algorithm

Symbol	Interpretation	Value
tol_1	Ratio of lengths, below which an edge is partitioned.	0.70
tol_2	Ratio between length of the largest edge and the sum of the other two lengths above which the largest edge is partitioned.	0.95
$h_{\min}$	Minimum edge length.	⊛

⊛ Problem data

Figure 5 shows the relevant data for the quasi-brittle cantilever beam. Our triangular shell element [40] is used to perform the discretization and independent nonlocal strains $\overline{\varepsilon}_{\text{lower}}$ and $\overline{\varepsilon}_{\text{upper}}$, see Eqs. (15–16), are used to correctly represent shell *bending*. To study the effect of mesh size, we use four values of h, as indicated in Fig. 5. A slight dependence on h is observable for higher values in Fig. 6a. In terms of element topology and for $h = 1.4286$ and $h = 2$ mm, it can be observed in Fig. 7 that triangular elements produce slightly stiffer results. In terms of step size, a clear effect can be noted in Fig. 7 which attenuates for $\Delta w \leq 5 \times 10^{-3}$ mm. Finally, the effect of L is also observable in Fig. 8, with larger values producing slightly more brittle results. We note that, although some dependence on the parameters in the force-displacement results can be observed, this dependence is generally mild and acceptable in most problems.

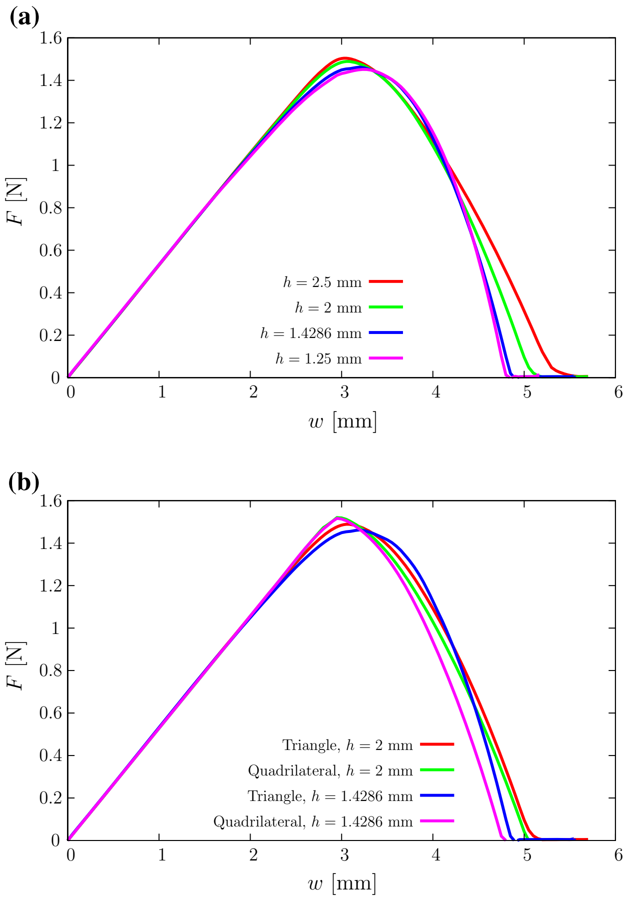

Fig. 6 Cantilever beam: effect of mesh size and element topology. **a** Effect of h, $L = 5$ mm. **b** Effect of element topology, $L = 5$ mm. (Color figure online)

Fig. 5 Cantilever beam: relevant geometry and properties

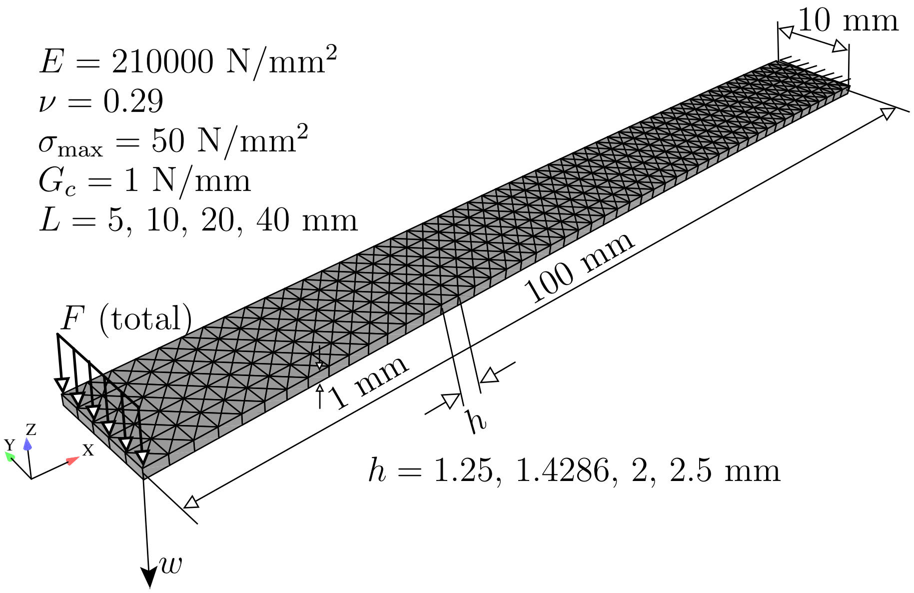

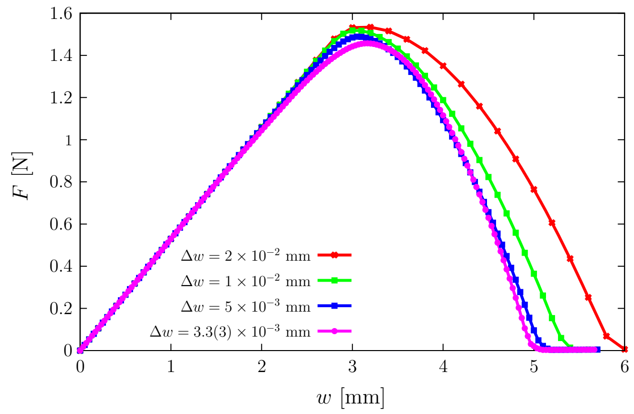

Fig. 7 Cantilever beam: effect of step size Δw. (Color figure online)

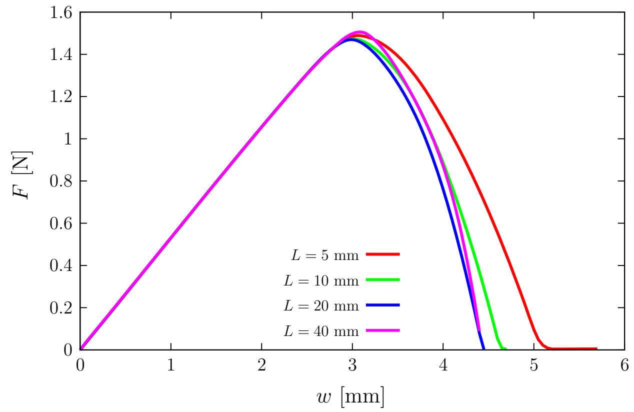

Fig. 8 Cantilever beam: effect of length parameter L. (Color figure online)

5.2 L-shaped panel

We now study a L-shaped panel introduced by Winkler [41] and numerically analyzed by Most and Bucher [42] using the *natural element method* and by Dumstorff and Meschke [43] using the *extended finite element method* (XFEM). More pertinent than the discretization method is the crack propagation technique used to define the path. In [42], the Authors used two distinct crack direction algorithms, namely the averaged Rankine criterion and the Erdogan-Sih LEFM criterion, cf [44], as each separately fails to predict the correct crack path in different problems. In [43], the Authors use a thermal tracking algorithm to estimate the crack lines. The present work avoids the need for a crack tracking algorithm, which is a considerable advantage.

Relevant data for this problem is shown in Fig. 9 agreeing with properties reported in [42]. Displacement control, with component v identified in Fig. 9, is used in the indicated *monitored* point with F being the corresponding force. Both crack path agreement and load/deflection results are scrutinized. We use three values of the initial characteristic mesh size $h = 8,\ 6$ and 4 mm with corresponding $h_{\min} = 5.333,\ 4.000$ and 2.666 mm.

In terms of crack-path prediction, we note that the finer mesh ($h = 4,\ h_{\min} = 2.666$ mm) gives rise to an almost-straight crack. Some difference is observable with respect to the experimental envelope. This is known to be caused by the use of a regularized continuum. Previous numerical experiments carried out by the Authors have provided a similar conclusion (see, e.g. [45]). With respect to the force-displacement results, we use the reported data from Most and Bucher [42] who use Carol et al. specific mixed-mode cohesive law [46]. The comparison is presented in Fig. 10. Satisfactory agreement is observed with respect to the results reported in [42] with a slight variation between the three mesh sizes.

5.3 Single edge notched beam: assessment of L, h and step size

An evaluation of the effect of L, h and step size is now performed. With this objective, the single edge notched (SEN) beam introduced by Schlangen (cf. [47]) is adopted using three distinct mesh densities with the same ratio $^{h_{\min}}/_{h} = 0.5325$. A description of this problem, with constitutive properties and boundary conditions is shown in Fig. 11. Three uniform meshes are adopted, with $h = 4$, 3 and 2 mm. In terms of remeshing, the corresponding $h_{\min}$ are 2.13, 1.6 and 1.07 mm. For the screened-Poisson equation we adopt four distinct values of L: $L = 5$, 10, 15 and 20 mm. The arc-length method is used in the solution, with monotonically increasing CMSD (crack mouth sliding displacement). The crack path reproduces closely the experimental envelope, as can be observed in Fig. 12; even near the support the experimental observations are adequately reproduced. A comparison with the experimental results and the DSDA method [48–50], along with a study of mesh and step size influence is performed. As can be observed in Fig. 13, excellent agreement is obtained, with very good insensitivity to the step size. In terms of length-scale L, we found that some sensitivity occurs for smaller values ($L = 5$ mm is particularly off) although values between 10 and 20 mm produce similar results. In terms of the effect of h, Fig. 14 shows an excellent robustness which is traditional of regularized solutions (cf. [31,33]).

5.4 Four-point single edge-notched beam

The four-point single-edge notched shear beam (SENS) problem by Arrea and Ingraffea [51] is described in Fig. 15. Properties coincide with the work of Most and Bucher [42], see also [52]. Here, we focus on the effect of mesh size h for fixed $^{h_{\min}}/_{h} = 0.5$. Four mesh sizes are adopted, correspond-

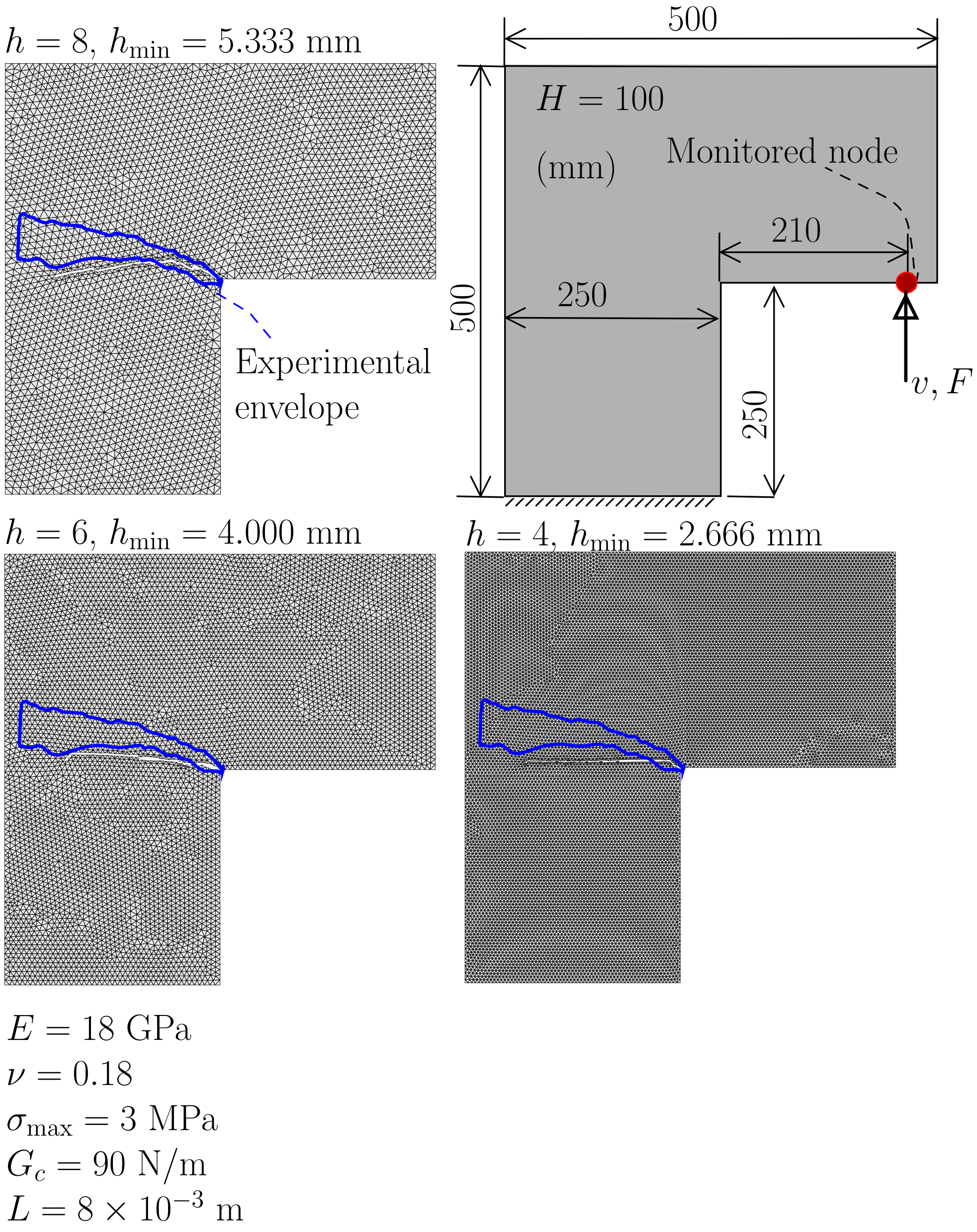

Fig. 9 L-shaped panel: geometry and relevant data

ing to edge lengths h: $h = 5,\ 6,\ 8$ and 10 mm. As in the SEN test, we use the CMSD as control variable (with each increment fixed as $\Delta\text{CMSD} = 1 \times 10^{-3}$). A comparison with the *meshless* results reported by Most and Bucher [42] and the reported experimental results is performed in Fig. 16 where, despite some difference between distinct meshes, reasonable agreement can be observed. Snap-back behavior in the $v - F$ diagram is shown in Fig. 17. Crack paths for four values of h are in excellent agreement with the experiments, as Fig. 18 shows. However, finer meshes tend to slightly reduce the crack path curvature, which can be observed for the case $h = 5$ mm.

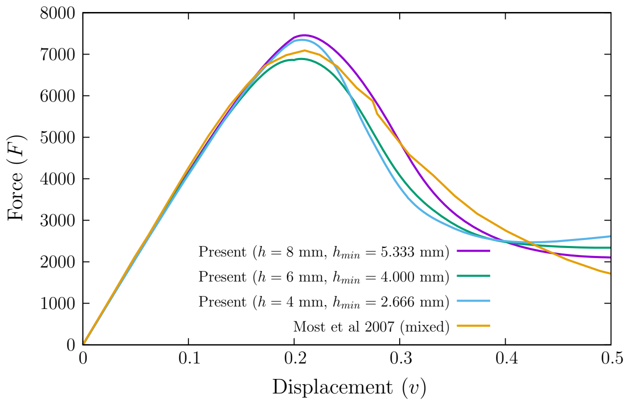

Fig. 10 L-shaped panel: v-F diagram. (Color figure online)

5.5 Crack growth in a four-point bending concrete beam: effect of $h_{\min}/h$

Concerning the crack path formation and robustness, the effect of $h_{\min}/h$ should be inspected. For this exercise we make use of the four-point bending concrete beam proposed by Bocca et al. [53]. The four-point bending beam problem consists of a bi-notched beam subjected to two point loads. The effect of size is inspected: two specimens with different dimensions are tested. From the set of specimens studied by Bocca et al. [53] we focus on specimens with $c/b = 0.8$, $b = 50$ and $b = 200$ mm, since these have reproducible experimental data. We use $L = 12$ mm for the larger specimen and $L = 3$ mm for the smaller one. We compare the crack paths and the force-displacement numerical results with those reported in [53]. It is worth noting that, using the cracking particle method, Rabczuk and Belytschko [54] obtained very good crack path predictions, although the force in the force-displacement diagram was higher than experimentally observed. In addition, with the particle methods, there is the problem of selecting the support dimension in the crack region. Relevant data is shown in Fig. 19, along with the contour plot of $\overline{\varepsilon}$. Crack paths and mesh size evolution are shown in Fig. 20 for the four values of $h_{\min}/h$. Below $h_{\min}/h = 0.495$, the crack path begins to exhibit the correct curvature and agreement with the experiments. In terms of analysis, for anti-symmetry reasons, we force the same mouth horizontal displacement at the edge of notches A and B: $\Delta u_B = \Delta u_A$. The relatively wide spread of experimental crack paths is typical and results from the use of six specimens of reference [53]. Experimentally, some residual crack evolution in the opposite direction of the final path was observed and we also obtained that effect. Force-displacement results are shown in Fig. 21 where a comparison with the measurements of Bocca et al. [53] and the cracking particle method of Rabczuk and Belytschko [54] is made.

6 Conclusions and extensions

By combining a staggered algorithm with the modified screened Poisson equation and adaptive mesh refinement, we successfully solved five problems in quasi-brittle fracture. Two main goals were achieved:

1. Crack path criteria are not required. Mesh refinement indirectly provides the crack path.
2. Cohesive laws are not required. A regularized continuum law, within a smeared model, is used which provides very

Fig. 11 Schlangen's SEN test: geometry, boundary conditions and material properties

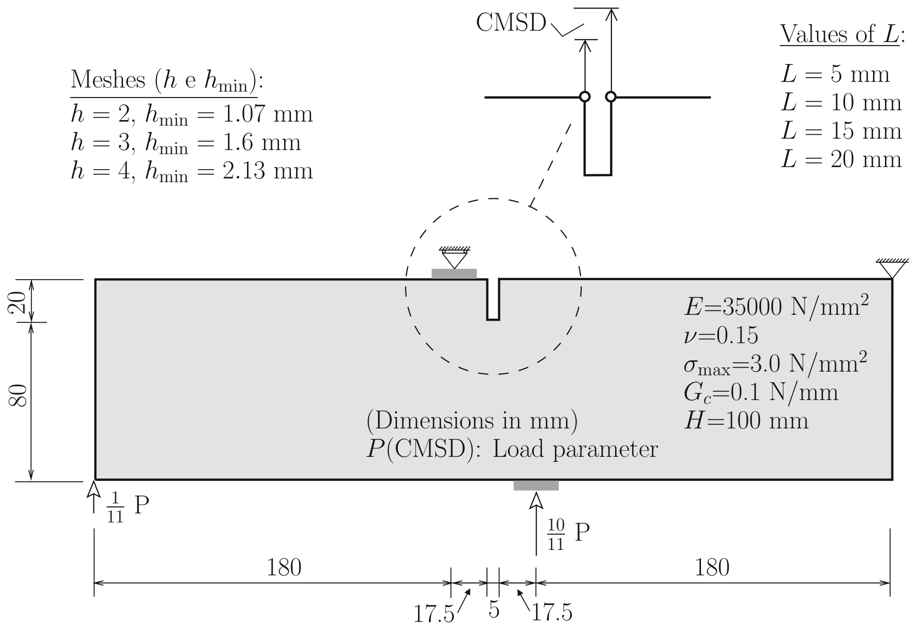

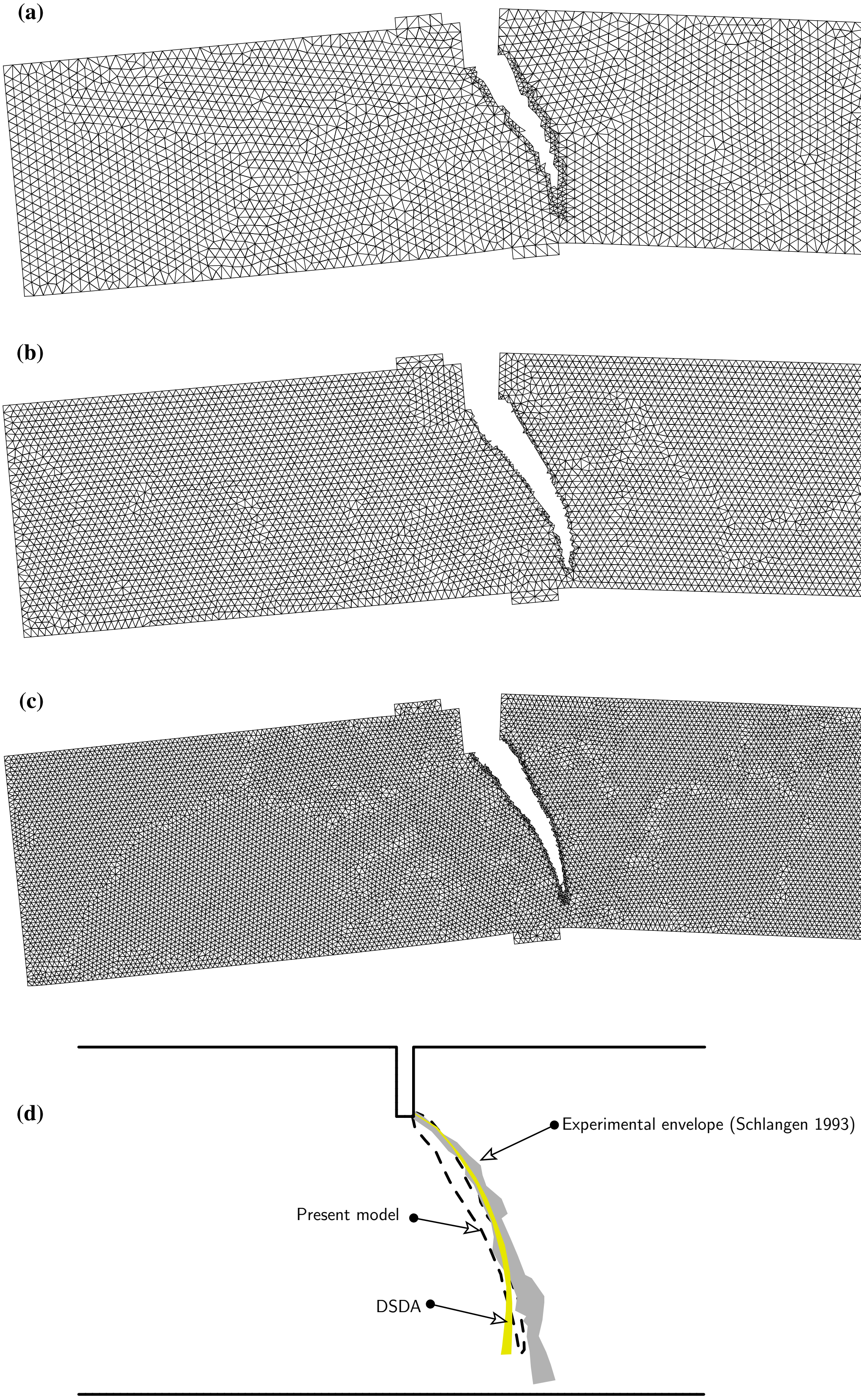

Fig. 12 Schlangen's SEN test: Deformed meshes for the three values of h. Elements with high values of d are removed. Crack path ($h = 2$ mm) compared with DSDA [50] (*yellow*) and the experimental results by Schlangen [47]. **a** $h = 4$ mm (magnified). $L = 10$ mm. **b** $h = 3$ mm (magnified). $L = 10$ mm. **c** $h = 2$ mm (magnified). $L = 10$ mm. **d** Crack path comparison. (Color figure online)

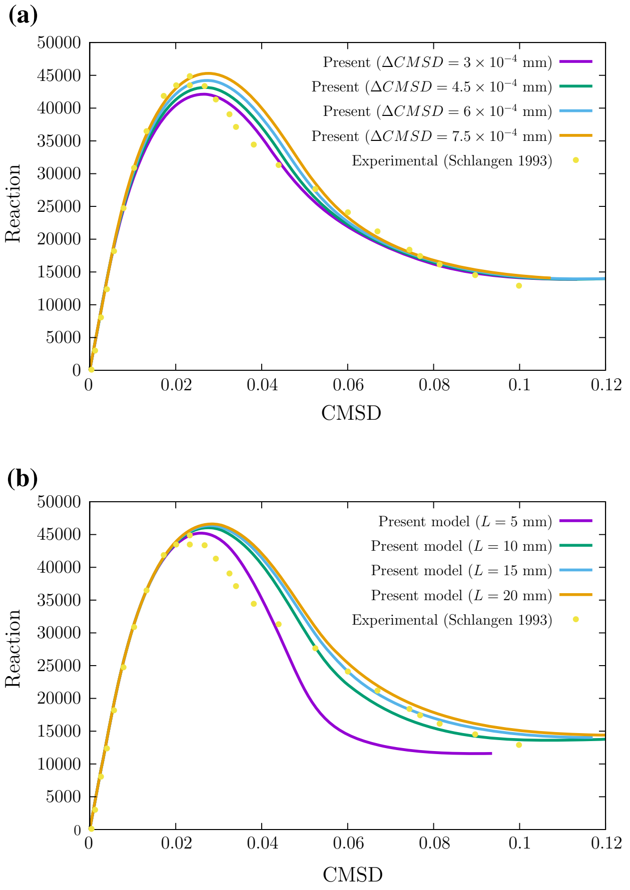

Fig. 13 Schlangen's SEN test: load-CMSD results: comparison with the experimental results by Schlangen [47] and effect of L and step size. **a** Load-CMSD results for four values of ΔCMSD. **b** Load-CMSD results for four values of L. (Color figure online)

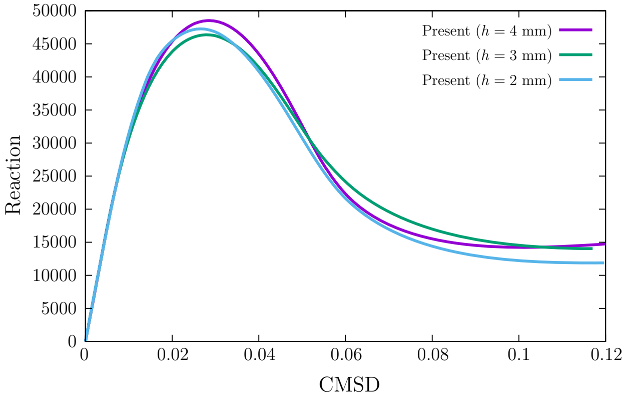

Fig. 14 Schlangen's SEN test: load-CMSD results: effect of mesh size h ($\Delta CMSD = 3 \times 10^{-4}$ mm, $L = 10$ mm). (Color figure online)

accurate results in terms of energy dissipation without the requisite of special surface elements.

Besides the usual mesh length h, which is required to solve any finite element problem, only two additional solution parameters are required: the non-local length L appearing in the screened-Poisson equation and also in the smeared model, which is applied in a staggered form, and the mesh refinement length h_{min}, controlling the subdivision of elements. When compared with enrichment methods or classical remeshing algorithms, we detected the following two shortcomings in the present technique:

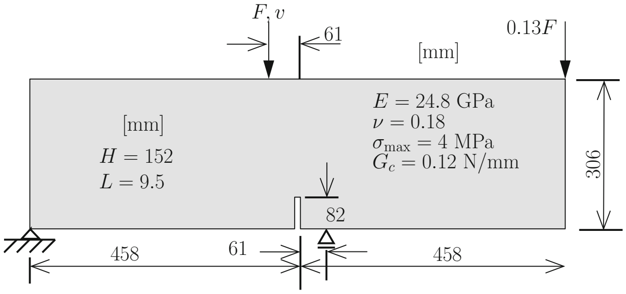

Fig. 15 SENS problem: relevant data and meshes

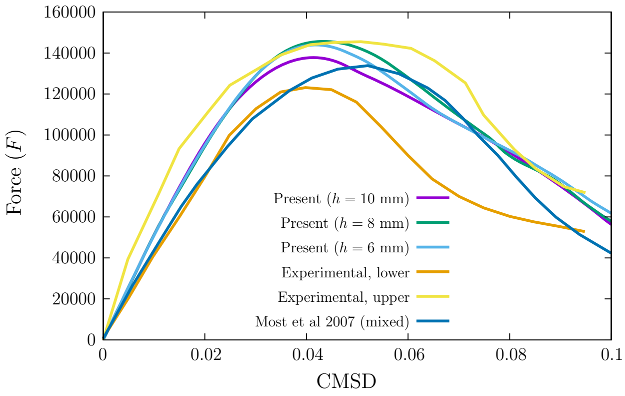

Fig. 16 SENS problem: Force-CMSD results: effect of mesh size h. Also shown are results from Most and Bucher [42] and the experimental results. (Color figure online)

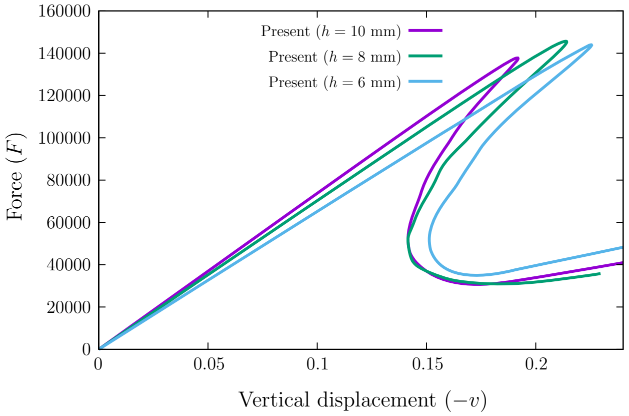

Fig. 17 SENS problem: Force-displacement results: effect of mesh size h. (Color figure online)

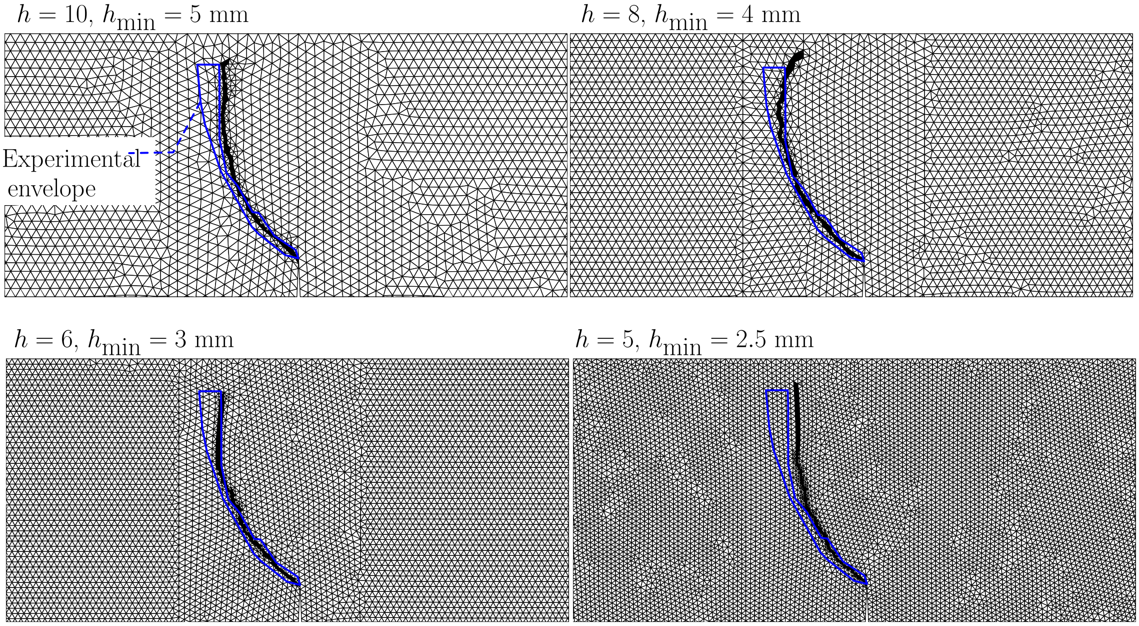

Fig. 18 SENS problem: Force-displacement results: effect of mesh size h

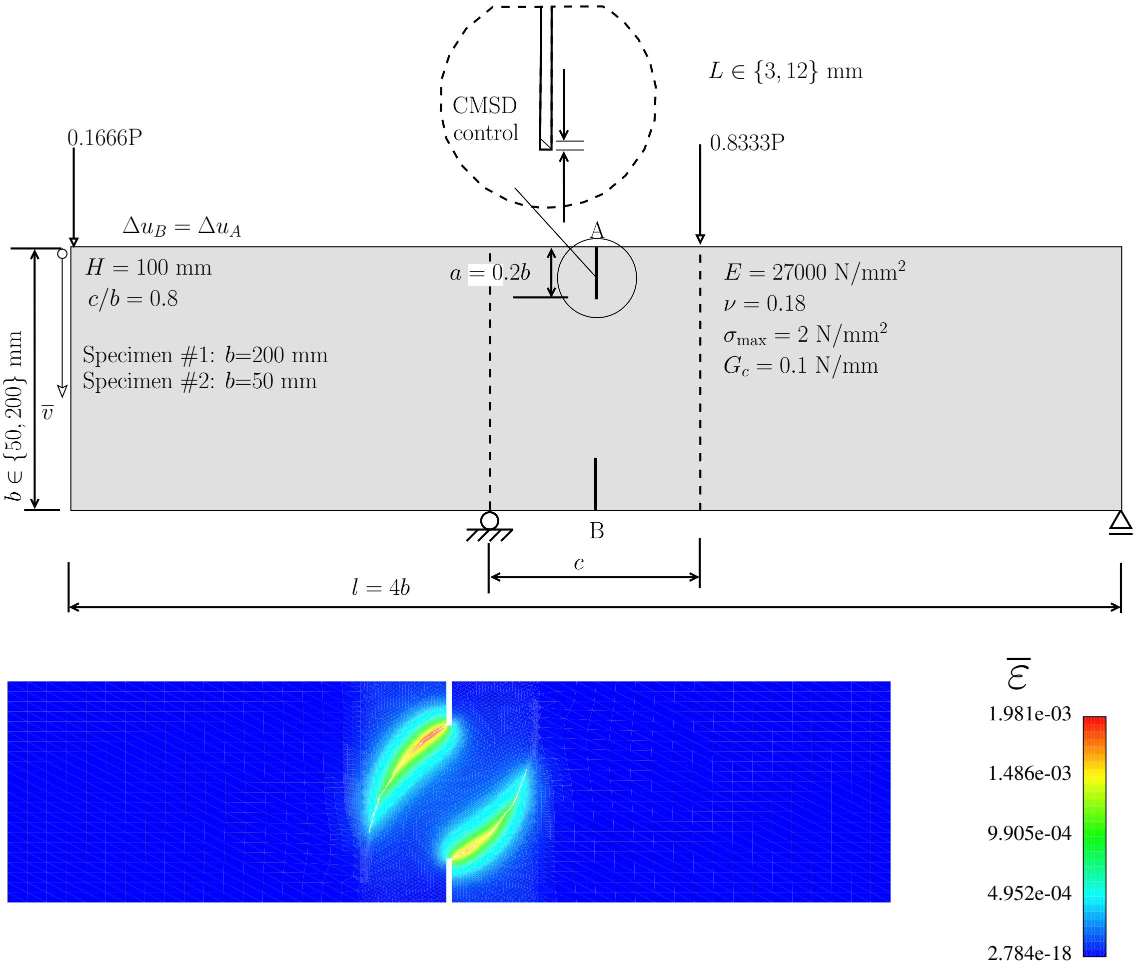

Fig. 19 Four-point bending of a concrete beam: geometry, boundary conditions, multipoint constraints ($\Delta u_B = \Delta u_A$) and material properties. Also shown is the contour plot for $\bar{\varepsilon}$. (Color figure online)

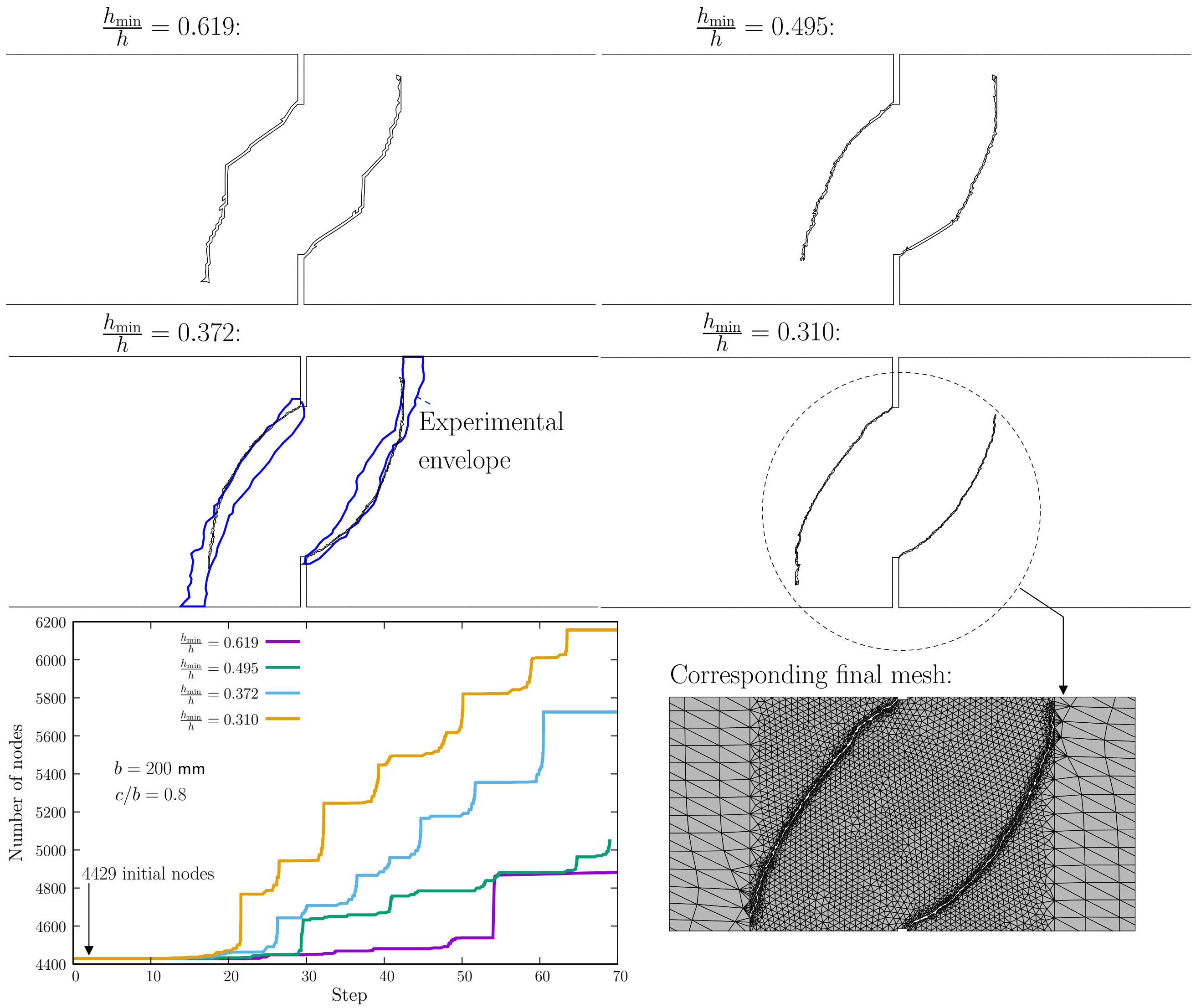

Fig. 20 Four-point bending of a concrete beam: crack paths compared with the envelope of experimental results by Bocca et al. [53]. The increase in the number of nodes is shown for four values of $h_{\min}/h$. (Color figure online)

1. Computational cost is comparatively high, since two analysis are performed, with the second involving regularization and equilibrium equations. Degrees-of-freedom also increase in the first stage of the analysis.
2. In the L-shaped panel there was some difficulty in reproducing the experimental crack path.

The two-stage algorithm introduced, consists of:

1. A local approach to fracture with local remeshing and global node repositioning. The only parameter in this stage is the minimum element size, $h_{\min}$. The purpose of this stage is to establish the appropriate mesh for the regularized problem.
2. A second stage which consists of a regularized continuum with a modified screened Poisson equation depending on L and a smeared model using the *same* parameter L.

Mostly good crack path agreement with quasi-brittle experiments was obtained. Good agreement in the force-deflection and force-CMSD results was also observed.

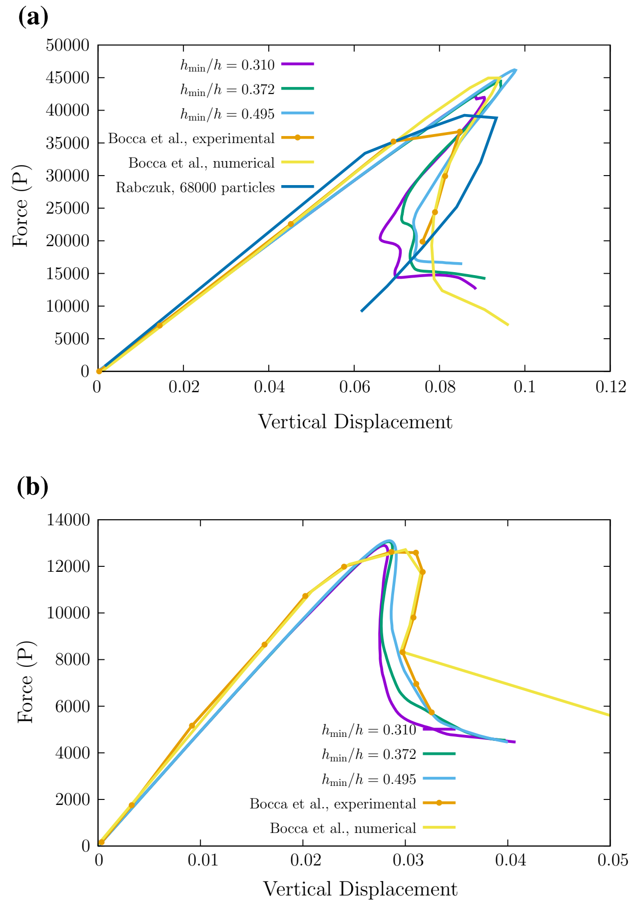

Fig. 21 Force-displacement results, compared with the results of Bocca et al. [53] and the cracking particle method of Rabczuk and Belytschko [54] (for the case $b = 200$ mm) with their 68,000 particle analysis. **a** $b = 200$ nm. **b** $b = 50$ nm. (Color figure online)

Concerning the extension to three-dimensional analysis, Eqs. (19) and (20) remain unchanged and only the remeshing algorithm described in Section differs 4 in terms of edge and face partitioning. The work of [55] on adaptive tetrahedron edge division is applicable.

References

1. Moës N, Dolbow J, Belytschko T (1999) A finite element method for crack growth without remeshing. Int J Numer Methods Eng 46:131–150
2. Oliver J (1995) Continuum modelling of strong discontinuities in solid mechanics using damage models. Comput Mech 17:49–61
3. Henshell RD, Shaw KG (1975) Crack tip elements are unnecessary. Int J Numer Methods Eng 9:1727–1742
4. Lasry D, Belytschko T (1988) Localization limiters in transient problems. Int J Solids Struct 24:581–597
5. Bittencourt TN, Wawrzynek PA, Ingraffea AR, Sousa JL (1996) Quasi-automatic simulation of crack propagation for 2D LEFM problems. Eng Fract Mech 55(2):321–334
6. Colombo D, Giglio M (2006) A methodology for automatic crack propagation modelling in planar and shell fe models. Eng Fract Mech 73:490–504
7. Karihaloo BL, Xiao QZ (2003) Modelling of stationary and growing cracks in FE framework without remeshing: a state-of-the-art review. Comput Struct 81:119–129
8. Loehnert S, Belytschko T (2007) A multiscale projection method for macro/microcrack simulations. Int J Numer Methods Eng 71:1466–1482
9. Moës N, Belytschko T (2002) Extended finite element method for cohesive crack growth. Eng Fract Mech 69:813–833
10. Nguyen-Xuan H, Liu GR, Nourbakhshnia N, Chen L (2012) A novel singular ES-FEM for crack growth simulation. Eng Fract Mech 84:41–66
11. Pierard O, Jin Y, Wyart E, Dompierre B, Bechet E (2016) Simulation of contact on crack lips and its influence on fatigue life prediction. In: Carpintieri A, Fatemi A, Navarro C (eds) International Conference on Multiaxial Fatigue and Fracture, ICMFF11, Seville. Fracture and structural integrity
12. Alfaiate J, Wells GN, Sluys LJ (2002) On the use of embedded discontinuity elements with crack path continuity for mode-I and mixed-mode fracture. Eng Fract Mech 69:661–686
13. Hansbo A, Hansbo P (2004) A finite element method for the simulation of strong and weak discontinuities in solid mechanics. Comput Methods Appl Mech Eng 193:3523–3540
14. Areias P, Rabczuk T (2013) Finite strain fracture of plates and shells with configurational forces and edge rotations. Int J Numer Methods Eng 94:1099–1122
15. Miehe C, Gürses E (2007) A robust algorithm for configurational-force-driven brittle crack propagation with $r-$adaptive mesh alignment. Int J Numer Methods Eng 72:127–155
16. Duflot M, Nguyen-Dang H (2004) A meshless method with enriched weight functions for fatigue. Int J Numer Methods Eng 59:1945–1961
17. Barbieri E, Petrinic N (2014) Three-dimensional crack propagation with distance-based discontinuous kernels in meshfree methods. Comput Mech 53(2):325–342
18. Peng X, Atroshchenko E, Kerfriden P, Bordas SPA (2016) Isogeometric boundary element methods for three dimensional static fracture and fatigue crack growth. Comput Methods Appl Mech Eng (in press)
19. Paulus CJ, Untereiner L, Courtecuisse H, Cotin S, Cazier D (2015) Virtual cutting of deformable objects based on efficient topological operations. Vis Comput 31:831–841
20. Bouchard PO, Bay F, Chastel Y (2003) Numerical modeling of crack propagation—implementation, techniques and comparison of different criteria. Comp Methods Appl Mech Eng 192(35–36):3887–3908
21. El Khaoulani R, Bouchard PO (2012) An anisotropic mesh adaptation strategy for damage and failure in ductile materials. Finite Elem Anal Des 59:1–10
22. Teng X, Wierzbicki T (2006) Evaluation of six fracture models in high velocity perforation. Eng Fract Mech 73:1653–1678
23. Oliver J (1989) A consistent characteristic length for smeared cracking models. Int J Numer Methods Eng 28:461–474
24. Etse G, Willam K (1999) Failure analysis of elastoviscoplastic material models. J Eng Mech 125:60–69
25. Schreyer HL, Chen Z (1986) One-dimensional softening with localization. J Appl Mech 53:791–797
26. Areias P. Simplas. http://home.uevora.pt/~pmaa/SimplasWebsite/Simplas.html
27. Lemaitre J (1996) A course on damage mechanics, 2nd edn. Springer, New York
28. Fetter AL, Walecka JD (2003) Theoretical mechanics of particles and continua. Courier Dover, New York

29. Ogden RW (1997) Non-linear elastic deformations. Dover Publications, New York
30. Mazars J (1984) Application de la mécanique de l'endommagement au comportement non linéaire et à la rupture du béton de structure. Thèse de Doctorat d'Etat, Université Paris VI, Paris
31. Peerlings RHJ, de Borst R, Brekelmans WAM, de Vree JHP (1996) Gradient enhanced damage for quasi-brittle materials. Int J Numer Methods Eng 39:3391–3403
32. Areias P, Dias-da-Costa D, Alfaiate J, Júlio E (2009) Arbitrary bi-dimensional finite strain cohesive crack propagation. Comput Mech 45(1):61–75
33. Areias PMA, César de Sá JMA, Conceição CA (2003) A gradient model for finite strain elastoplasticity coupled with damage. Finite Elem Anal Des 39:1191–1235
34. de Borst R, Pamin J, Geers MGD (1999) On coupled gradient-dependent plasticity and damage theories with a view to localization analysis. Eur J Mech A 18:939–962
35. Geers MGD, de Borst R, Brekelmans WAM, Peerlings RHJ (1998) Strain-based transient-gradient damage model for failure analysis. Comput Methods Appl Mech Eng 160:133–153
36. Wolfram Research Inc. Mathematica (2007)
37. Korelc J (2002) Multi-language and multi-environment generation of nonlinear finite element codes. Eng Comput 18(4):312–327
38. Belytschko T, Liu WK, Moran B (2000) Nonlinear finite elements for continua and structures. Wiley, New York
39. Frey PJ, George P-L (2000) Mesh generation: application to finite elements. Hermes Science, Oxford
40. Areias P, Garção J, Pires EB, Barbosa JI (2011) Exact corotational shell for finite strains and fracture. Comput Mech 48:385–406
41. Winkler BJ (2001) Traglastuntersuchungen von unbewehrten und bew. Betonstrukturen auf der Grundlage eines objektiven Werkstoffgesetzes für Beton. PhD thesis, University of Innsbruck, Innrain 52, 6020 Innsbruck
42. Most T, Bucher C (2006) Energy-based simulation of concrete cracking using an improved mixed-mode cohesive crack model within a meshless discretization. Int J Numer Anal Met 31:285–305
43. Dumstorff P, Meschke G (2007) Crack propagation criteria. Int J Numer Anal Met 31:239–259
44. Erdogan F, Sih GC (1963) On the crack extension in plates under plane loading and transverse shear. J Bas Eng 85:519–527
45. Areias P, Msekh MA, Rabczuk T (2016) Damage and fracture algorithm using the screened poisson equation and local remeshing. Eng Fract Mech 158:116–143
46. Carol I, Prat PC, López CM (1997) Normal/shear cracking model: application to discrete crack analysis. J Eng Mech 123:765–773
47. Schlangen E (1993) Experimental and numerical analysis of fracture processes in concrete. PhD thesis, Delft
48. Alfaiate J, Simone A, Sluys LJ (2003) A new approach to strong embedded discontinuities. In: Bicanic N, de Borst R, Mang H, Meschke G (eds) Computational Modelling of Concrete Structures, EURO-C 2003. St. Johann im Pongau
49. Areias PMA, César de Sá JMA, Conceição António CA, Carneiro JASAO, Teixeira VMP (2004) Strong displacement discontinuities and Lagrange multipliers in the analysis of finite displacement fracture problems. Comput Mech 35:54–71
50. Dias-da-Costa D, Alfaiate J, Sluys LJ, Júlio E (2009) A discrete strong discontinuity approach. Eng Fract Mech 76(9):1176–1201
51. Arrea M, Ingraffea RA (1982) Mixed-mode crack propagation in mortar and concrete. Technical Report Report 81-13, Cornell University, Department of Structural Engineering
52. Areias PMA, Belytschko T (2005) Analysis of three-dimensional crack initiation and propagation using the extended finite element method. Int J Numer Methods Eng 63:760–788
53. Bocca P, Carpinteri A, Valente S (1991) Mixed mode fracture of concrete. Int J Solids Struct 27(9):1139–1153
54. Rabczuk T, Belytschko T (2004) Cracking particles: a simplified meshfree method for arbitrary evolving cracks. Int J Numer Methods Eng 61:2316–2343
55. Ruprecht D, Müller H (1998) A scheme for edge-based adaptive tetrahedron subdivision. In: Hege H-C, Polthier K (eds) Mathematical visualization: algorithms., Applications and numericsSpringer, Berlin, pp 61–70